Supporting Information

Molecular Water Oxidation Catalysis by Zwitterionic Carboxylate Bridge-Functionalized Bis-NHC Iridium Complexes

Raquel Puerta-Oteo, M. Victoria Jiménez, and Jesús J. Pérez-Torrente**

Department of Inorganic Chemistry, Instituto de Síntesis Química y Catálisis Homogénea (ISQCH-CSIC). University of Zaragoza-CSIC, Facultad de Ciencias, C/ Pedro Cerbuna, 12, 50009 Zaragoza, Spain.

Table of contents:

1.- Preliminary tests on water oxidation catalysis by [Cp*IrCl{(MeIm)$_2$CHCOO}] (1).

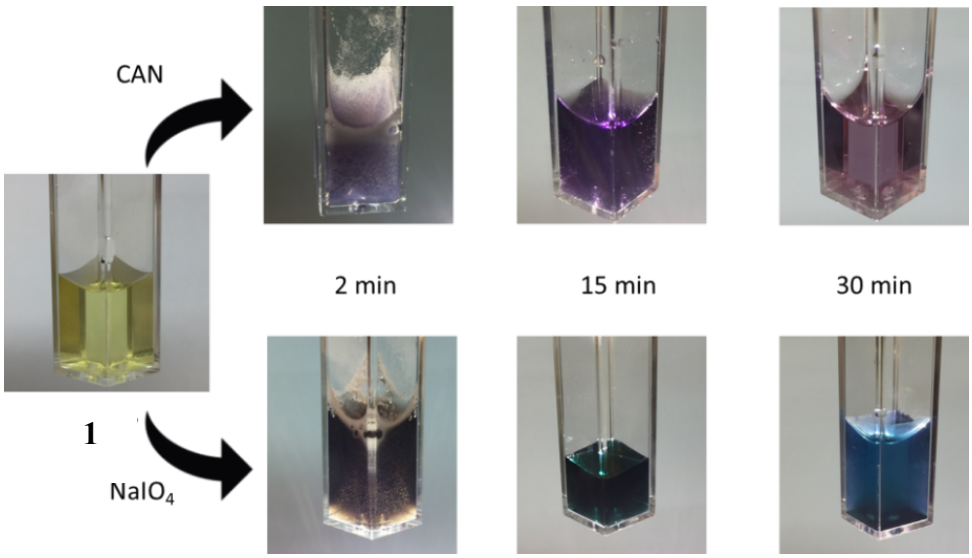

Figure S1. Qualitative tests for water oxidation catalysis performed with catalyst precursor [Cp*IrCl{(MeIm)$_2$CHCOO}] (**1**) using CAN and $NaIO_4$ as sacrificial oxidants.

2.- Catalytic activity for water oxidation of iridium catalyst precursors 1-7.

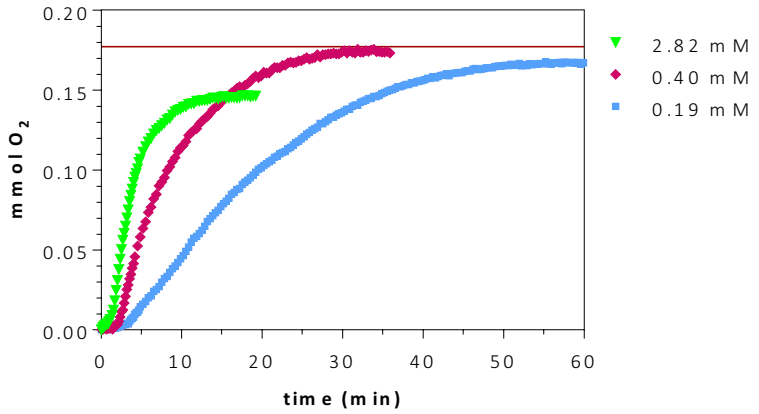

Figure S2. Plot of O_2(g) *vs*. time at various concentrations of complex [Ir(cod){(MeIm)$_2$CHCOO}] (**4**) (Table 1, entries 12-14). The produced oxygen in all the catalytic tests is consistent with the stoichiometric limit of added CAN (horizontal line).

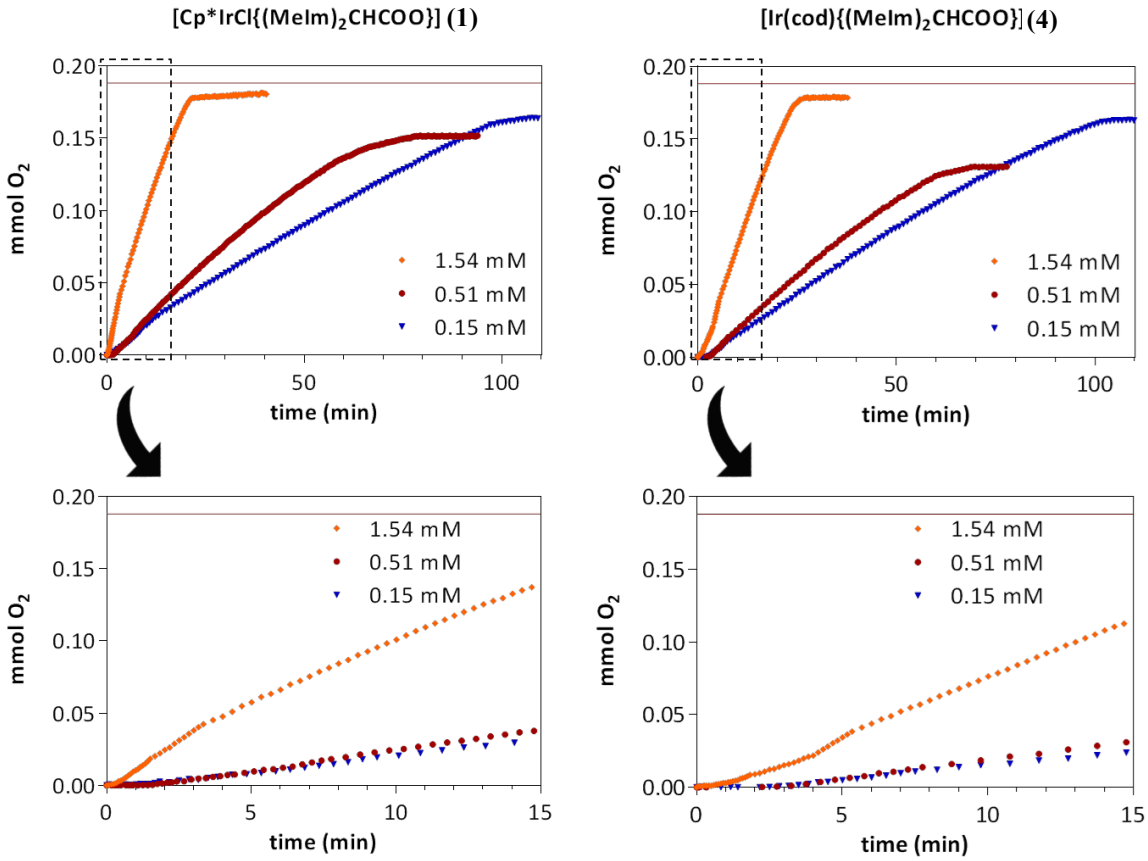

Figure S3. Plot of mmol of O_2(g) *vs*. time at various concentrations of complexes [Cp*IrCl{(MeIm)$_2$CHCOO}] (**1**) and [Ir(cod){(MeIm)$_2$CHCOO}] (**4**) (Table 2, entries 1-6) with enlarged plots of the boxed region showing the oxygen evolution at short reaction times. The produced oxygen in all the catalytic tests is consistent with the stoichiometric limit of added $NaIO_4$ (horizontal line).

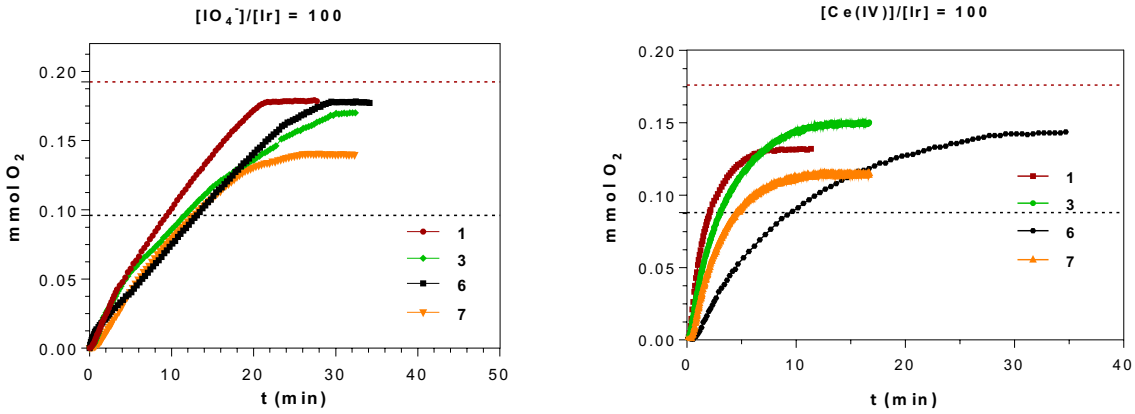

Figure S4. Plot of O_2(g) *vs*. time for iridium complexes **1**, **3**, **6** and **7** (Table 3, entries 1-8).

3.- Kinetic studies on water oxidation catalysis by catalyst precursors 1 and 4.

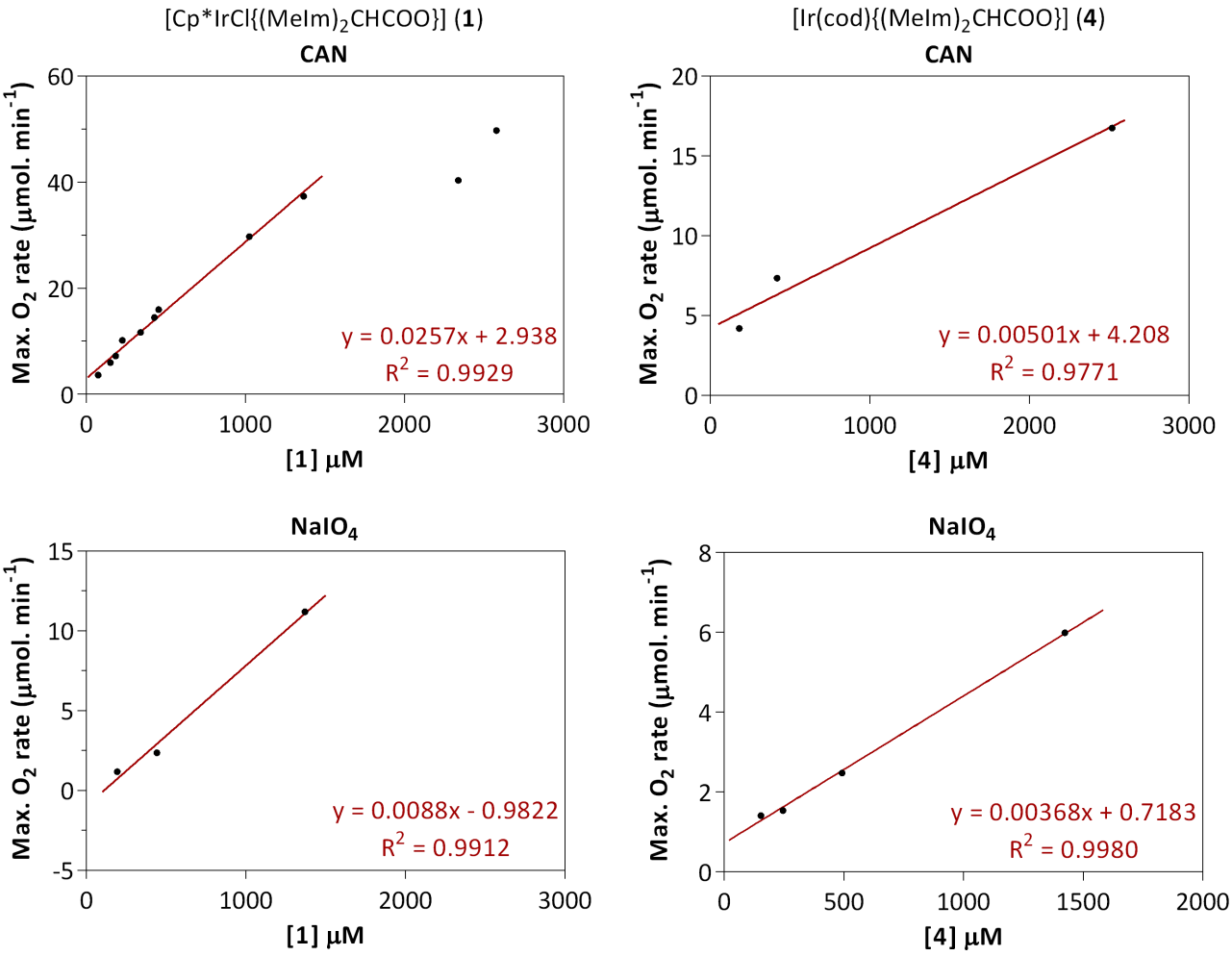

Figure S5. Plots of maximum rates of O_2(g) evolution determined at 20% conversion of the sacrificial oxidant (CAN and $NaIO_4$) *vs*. concentration of catalyst (**1** and **4**).

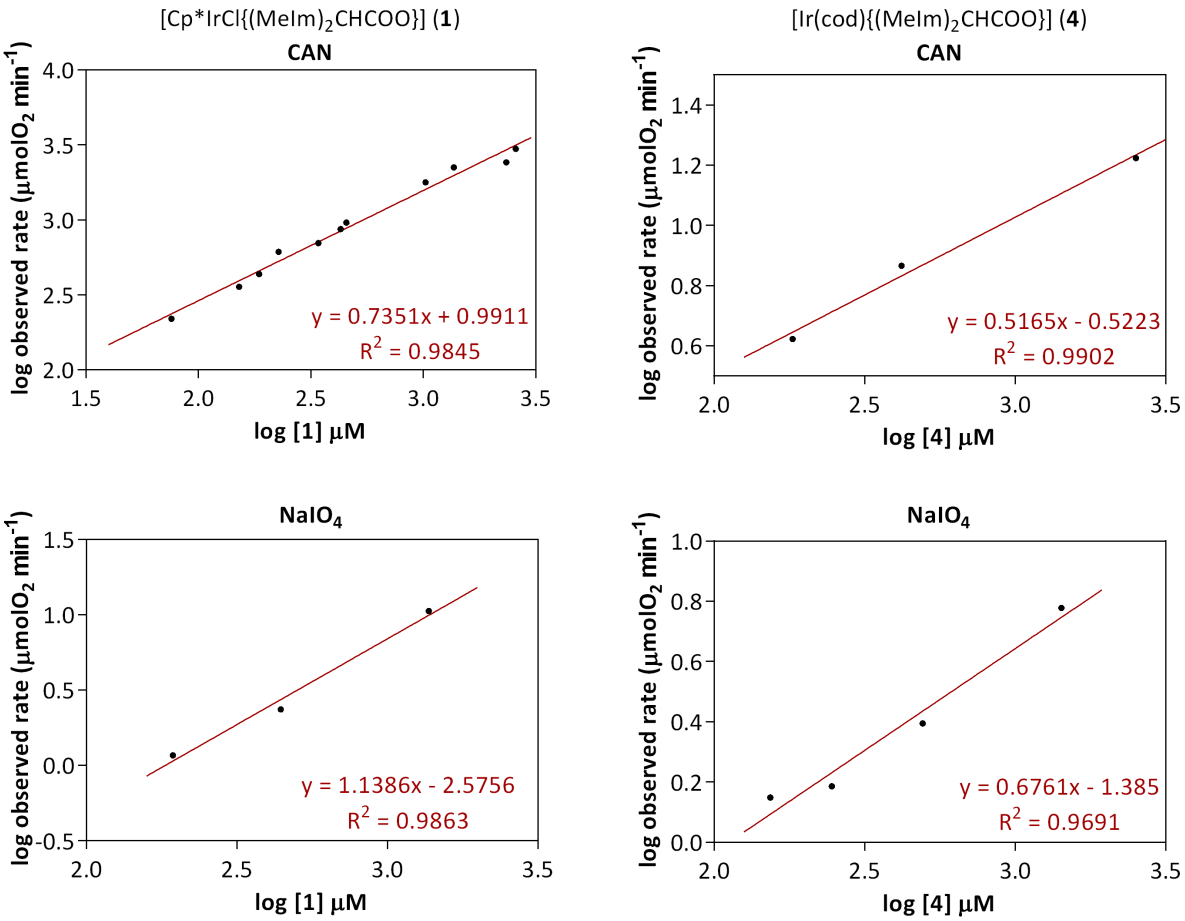

Figure S6. log(rate)-log[Ir] plots for catalysts **1** and **4** (CAN and $NaIO_4$) and the corresponding linear fits.

Table S1. Determined reaction order in catalyst for water oxidation by catalyst precursors **1** and **4**.

	CAN	$NaIO_4$
[Cp*IrCl{(MeIm)$_2$CHCOO}] (**1**)	0.73	1.14
[Ir(cod){(MeIm)$_2$CHCOO}] (**4**)	0.52	0.67

4.- Multi-step CAN-driven water oxidation by catalyst precursor 1.

Table S2. Multi-step CAN-driven water oxidation catalysis by [Cp*IrCl{(MeIm)$_2$CHCOO}] (**1**).[a]

Entry	[Ir] (mM)	[CAN] (mM)	[CAN]/[Ir]	mmol O_2	TON	TOF_{50} (h^{-1}) [b]	yield (%)
1	0.40	283	700	0.174	162	726	98
2	0.22	157	700	0.174	162	348	98
3	0.16	112	700	0.134	125	175	76

[a] Reaction carried out in 2.5 mL degassed water (pH = 1.0) in a thermostatic bath at 300 K, $[\mathbf{1}]_o$ = 0.43 mM, $[CAN]_o \approx$ 283 mM. Oxygen evolution after two consecutive additions of 2 mL of 351 mM solution of CAN (0.70 mmol). Final solution volume = 6.5 mL.

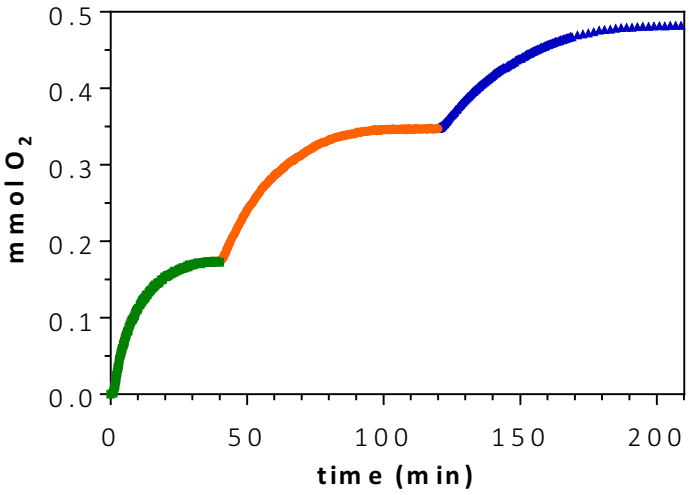

Figure S7. Oxygen production after two consecutive additions of 2 mL of 350 mM solution of CAN (0.70 mmol) to an initial solution of [Cp*IrCl{(MeIm)$_2$CHCOO}] (**1**): $[\mathbf{1}]_o$ = 0.43 mM, $[CAN]_o$ = 283 mM (2.5 mL, pH = 1.0) at 300 K.

5.- CAN-driven water oxidation by catalyst precursors 1 and 4: GC-MS analysis.

GC-MS spectrum of the gas phase after water oxidation catalysis by the catalytic systems **1**/CAN and **4**/CAN showed four main peaks that were assigned to: Ar (*m/z* 40), O_2 (*m/z* 32), N_2 (*m/z* 28) and CO_2 (*m/z* 44). N_2 comes from traces of air present in the needle of the micro-syringe as it was corroborated by a blank test of the Ar gas employed in the catalysis, which showed peaks assigned to Ar, N_2 and O_2 in the ratio corresponding to the composition of air (N_2/O_2 = 3.7). The presence of CO_2 was attributed to the degradation of the hydrocarbon ligands of the catalyst precursors.

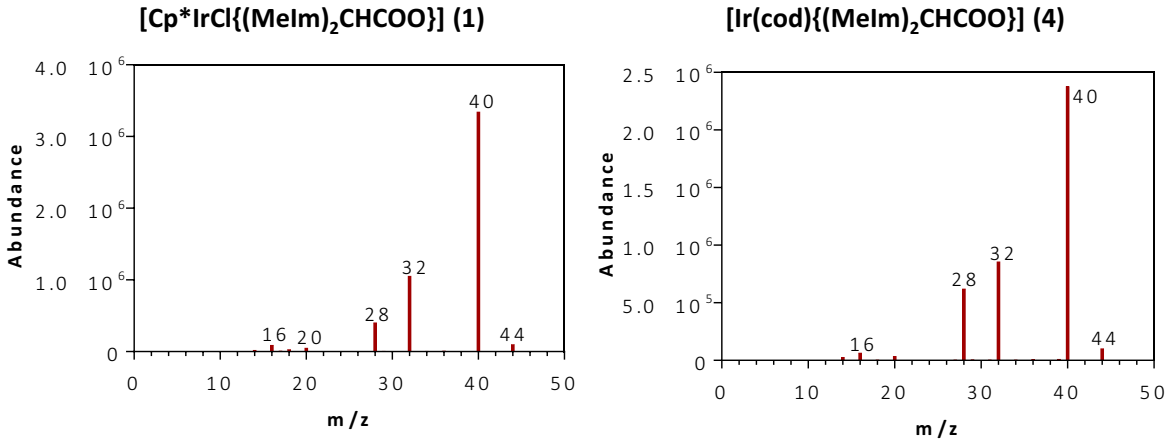

Figure S8. Representative GC-MS analysis of the headspace of the micro-reactor after CAN-driven water oxidation by catalysts precursors [Cp*IrCl{(MeIm)$_2$CHCOO}] (**1**) and [Ir(cod){(MeIm)$_2$CHCOO}] (**4**).

6.- DLS studies on water oxidation driven by CAN and $NaIO_4$ by catalyst precursors 1 and 4.

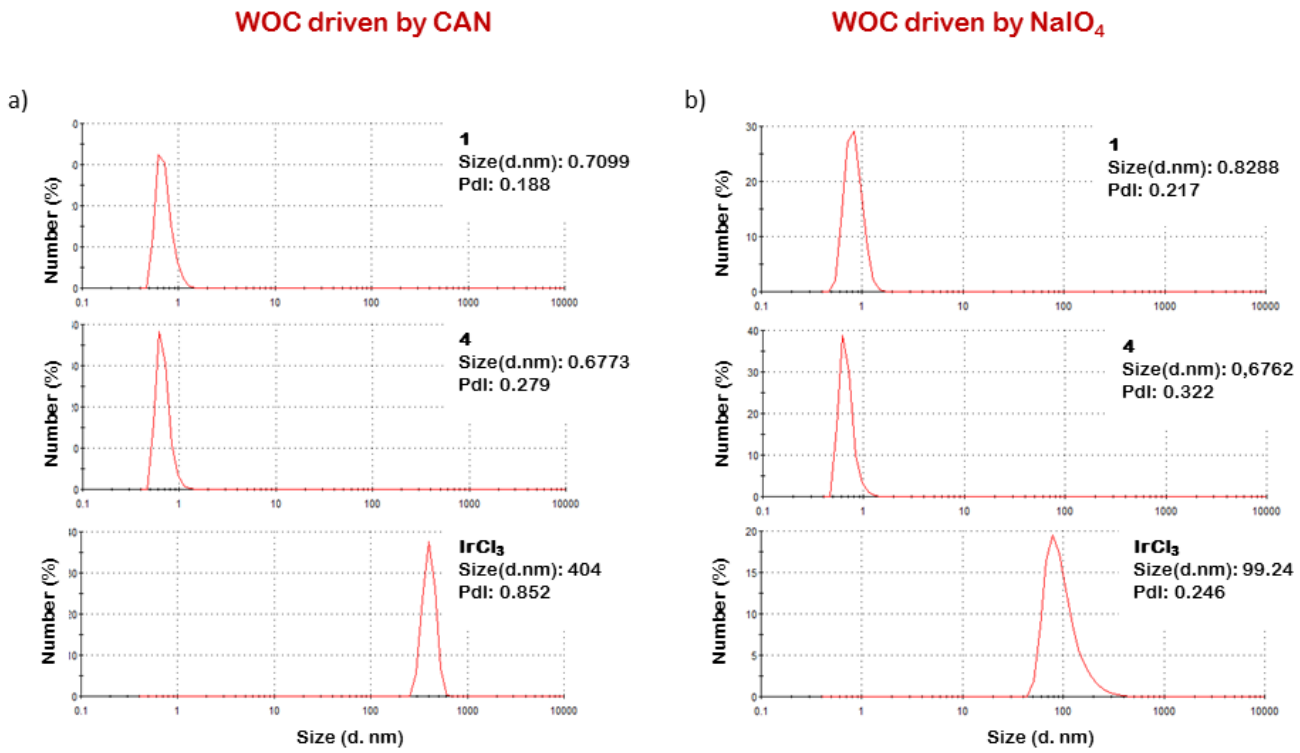

Figure S9. DLS response (by percentage of number) for aqueous solutions of **1**, **4** and **$IrCl_3$** (2.82 mM) after water oxidation catalysis. a) [CAN]/[Ir] = 100; b) [$NaIO_4$]/[Ir] = 100. Although no precipitate was observed all the solutions were filtered with a 0.22 μm Teflon filter to remove any dust particles.

7.- ^{1}H NMR studies on consecutive additions of CAN and $NaIO_4$ to catalyst precursor 1.

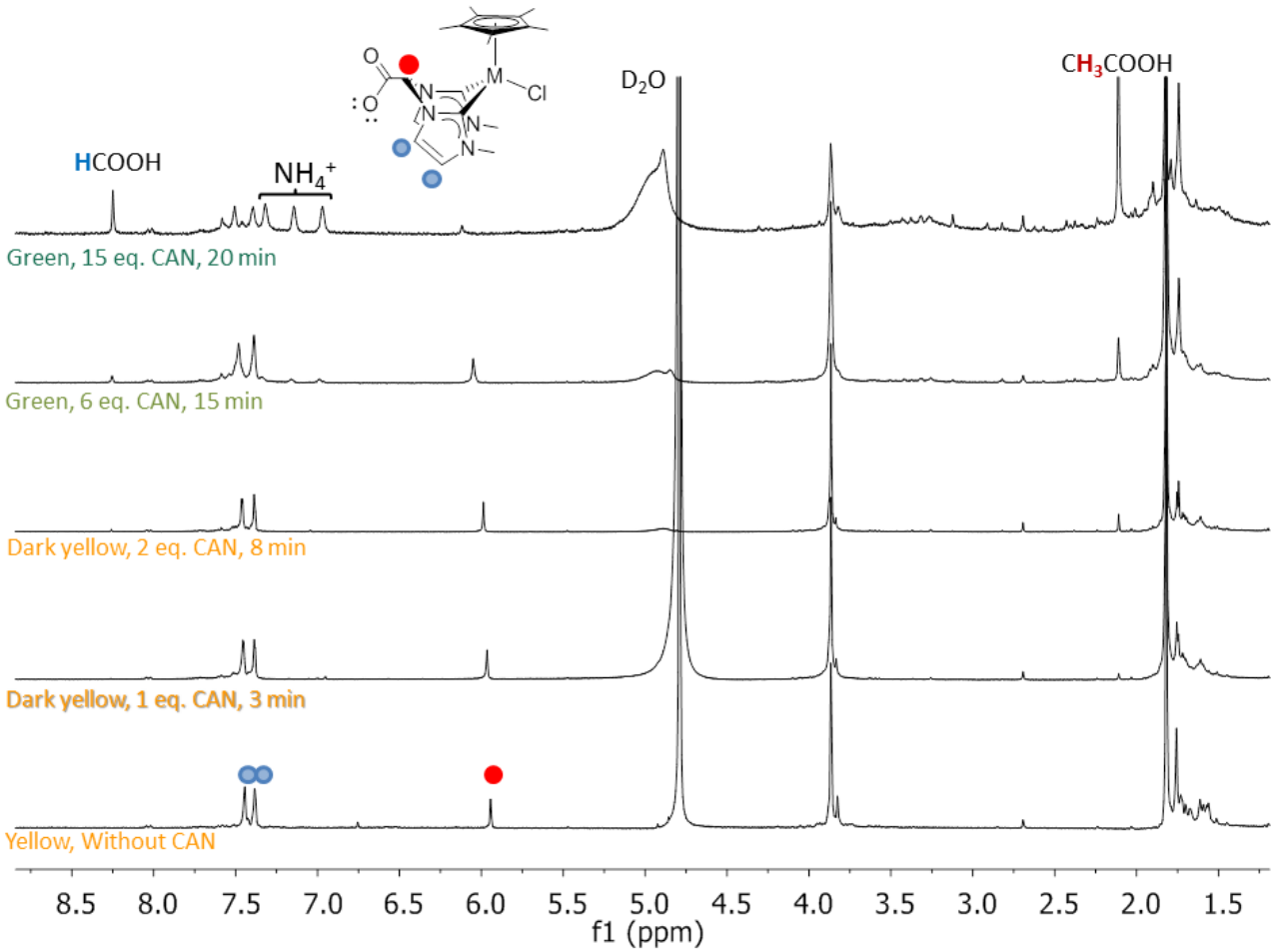

Figure S10. Evolution of ^{1}H NMR spectra (D_2O, 298K) of a solution of [Cp*IrCl{$(MeIm)_2CHCOO$}] (**1**) (60 mM) after consecutive additions of solid CAN (blue circles, down-field bis-NHC resonances of **1**).

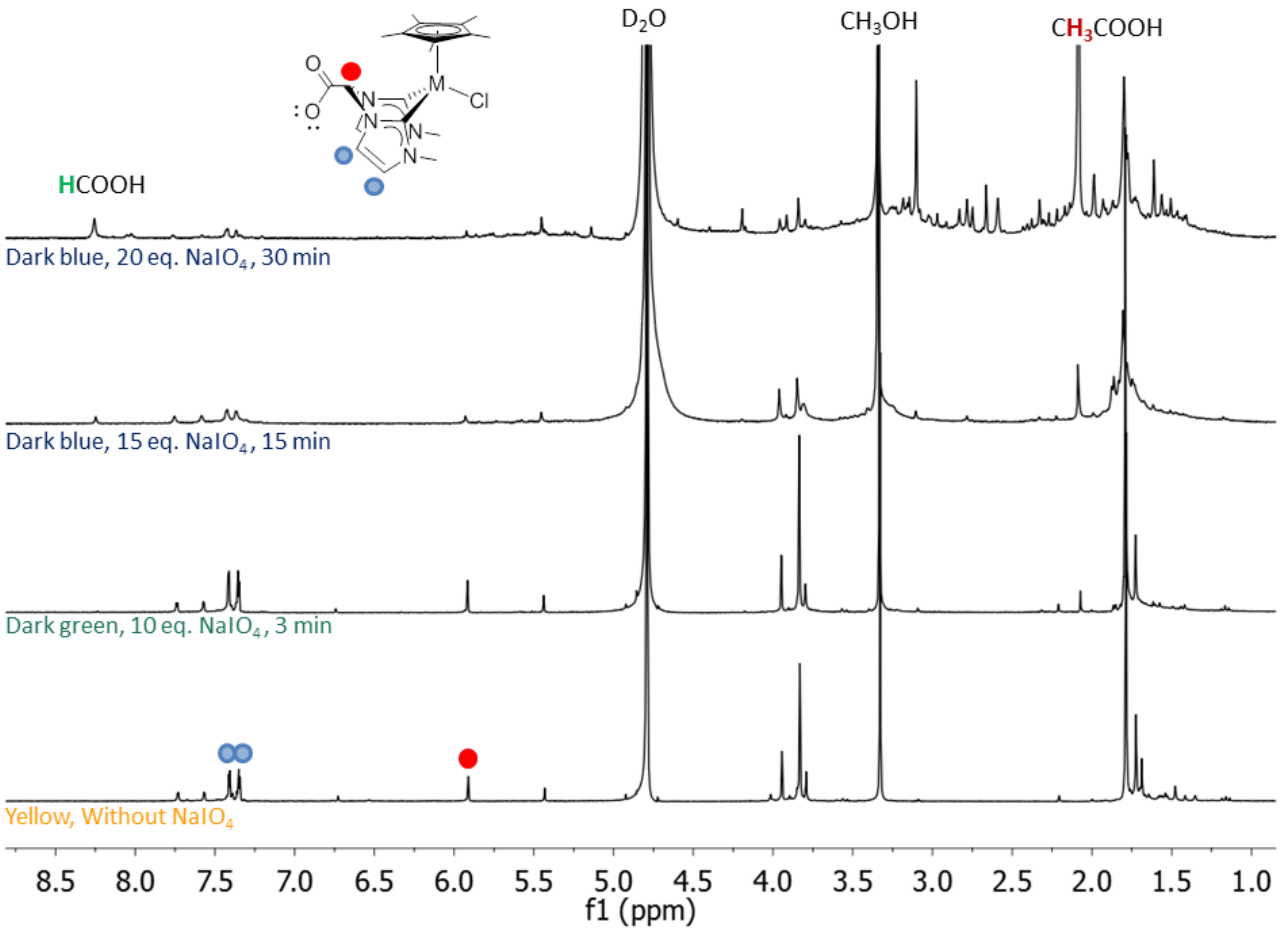

Figure S11. Evolution of ^{1}H NMR spectra (D_2O, 298K) of a solution of [Cp*IrCl{$(MeIm)_2CHCOO$}] (**1**) (60 mM) after consecutive additions of solid $NaIO_4$ (blue circles, down-field bis-NHC resonances of **1**).

8.- ^{1}H NMR spectra on consecutive additions of CAN to catalyst precursor 4 at pH = 1.

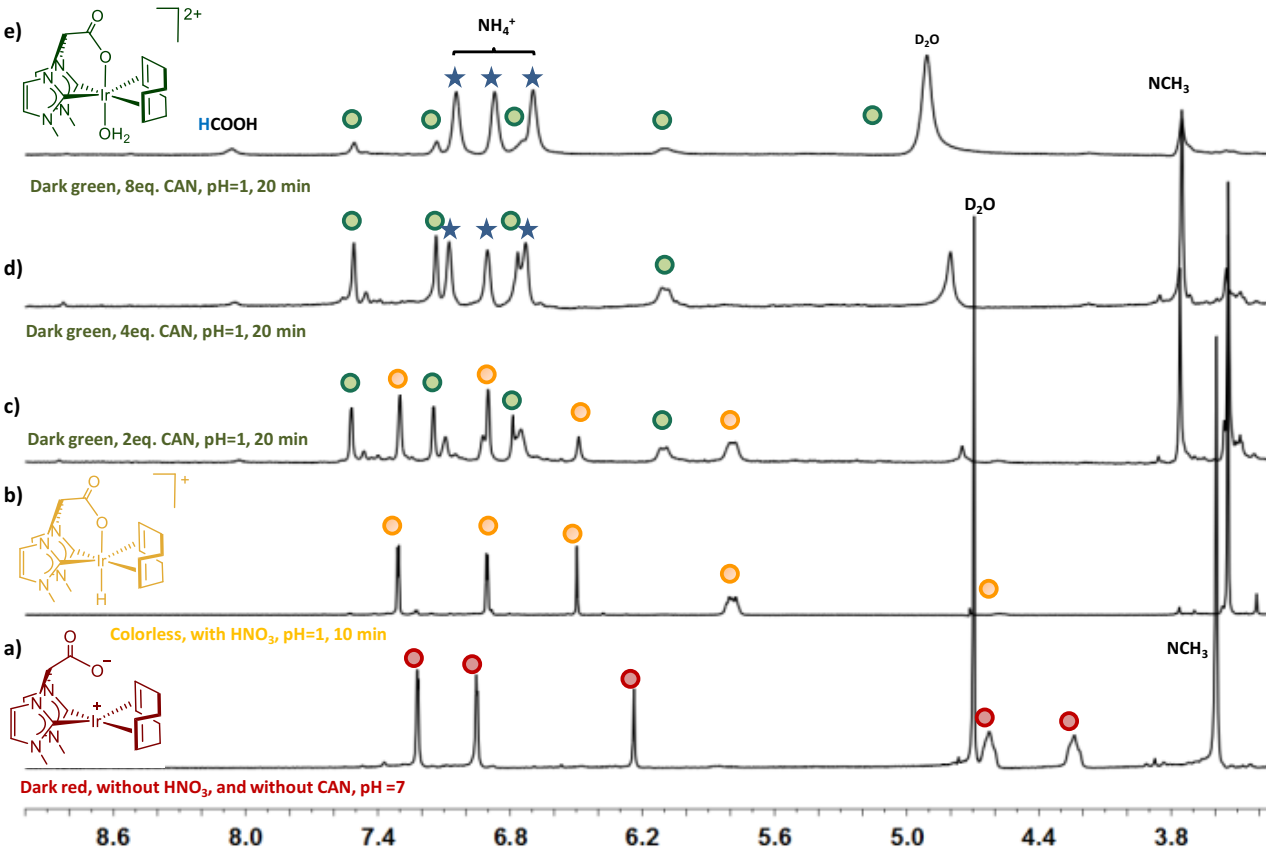

Figure S12. Evolution of the ^{1}H NMR spectra (D_2O, pH = 1, 0.1 M HNO_3, 298K) of a solution of [Ir(cod){$(MeIM)_2CHCOO$}] (**4**) (60 mM) after consecutive additions of solid CAN.

9.- Spectroscopic characterization of compounds 8 and 10.

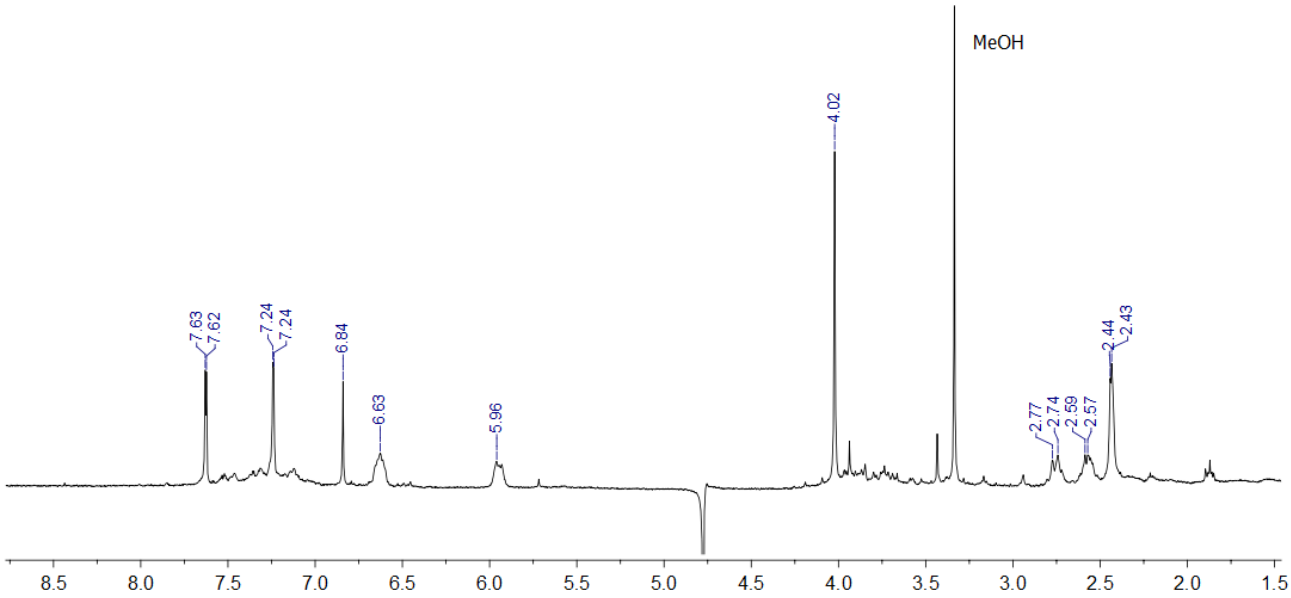

Figure S13. ^{1}H-Presat NMR (D_2O, 298K) of [Ir(OH)(cod){$(MeIm)_2CHCOO$}]IO_3 (**8**).

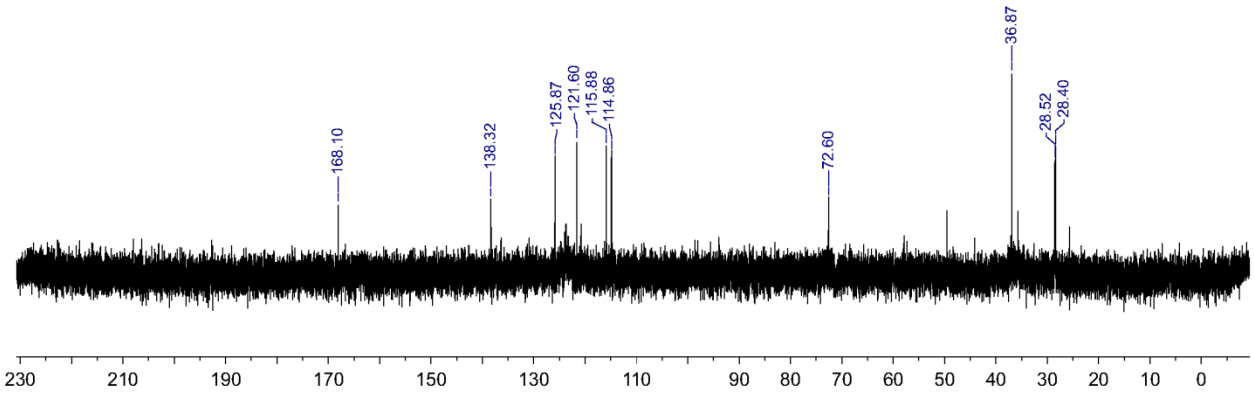

Figure S14. ^{13}C{^{1}H} NMR (D_2O, 298K) of [Ir(OH)(cod){$(MeIm)_2CHCOO$}]IO_3 (**8**).

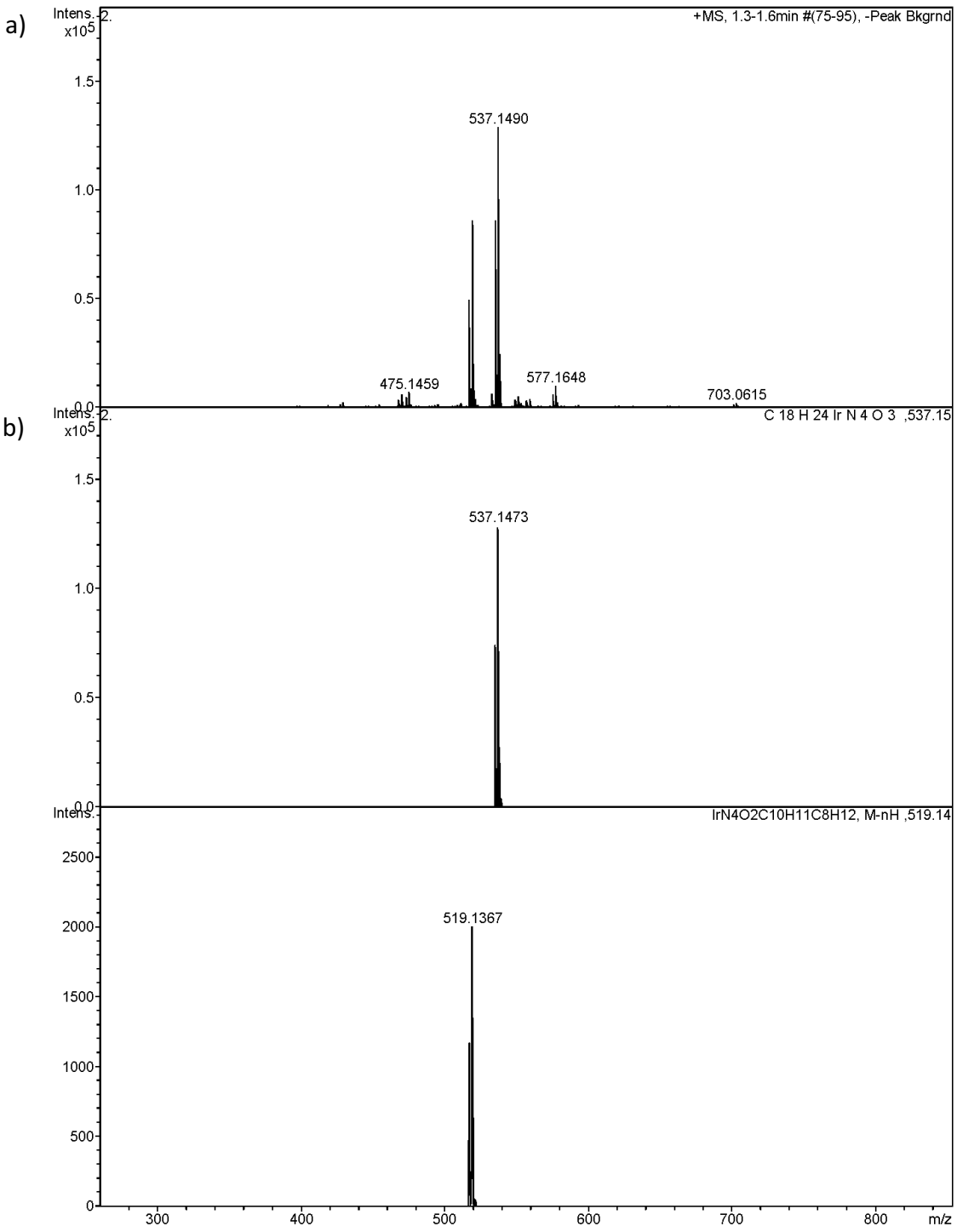

Figure S15. a) HRESI+-MS spectrum of **8**, b) Isotopic pattern for the most significant identified peaks.

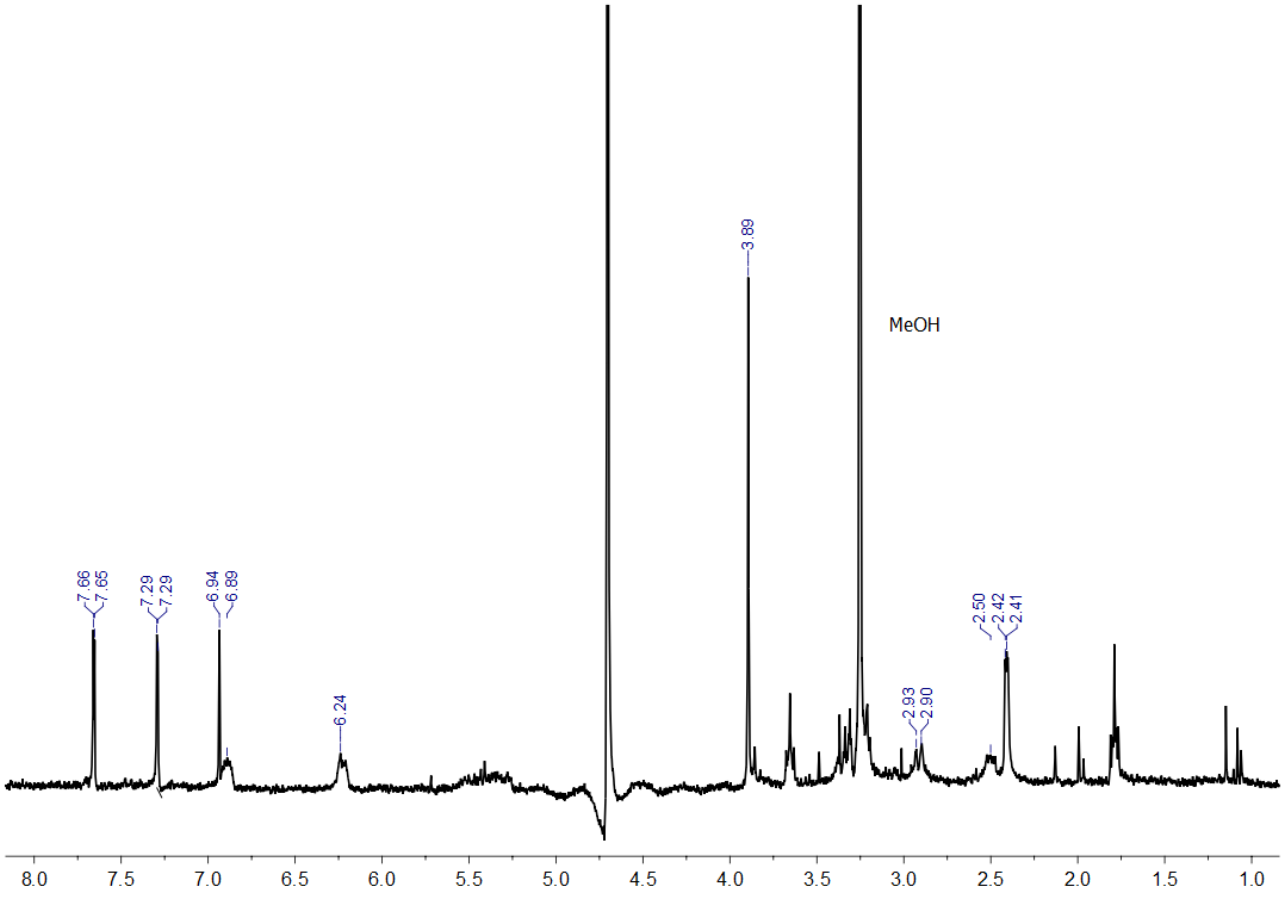

Figure S16. ^{1}H-presat NMR (D_2O, 298K) of $[Ir(H_2O)(cod)\{(MeIm)_2CHCOO\}]X_2$ (X = IO_3/NO_3) (**10**).

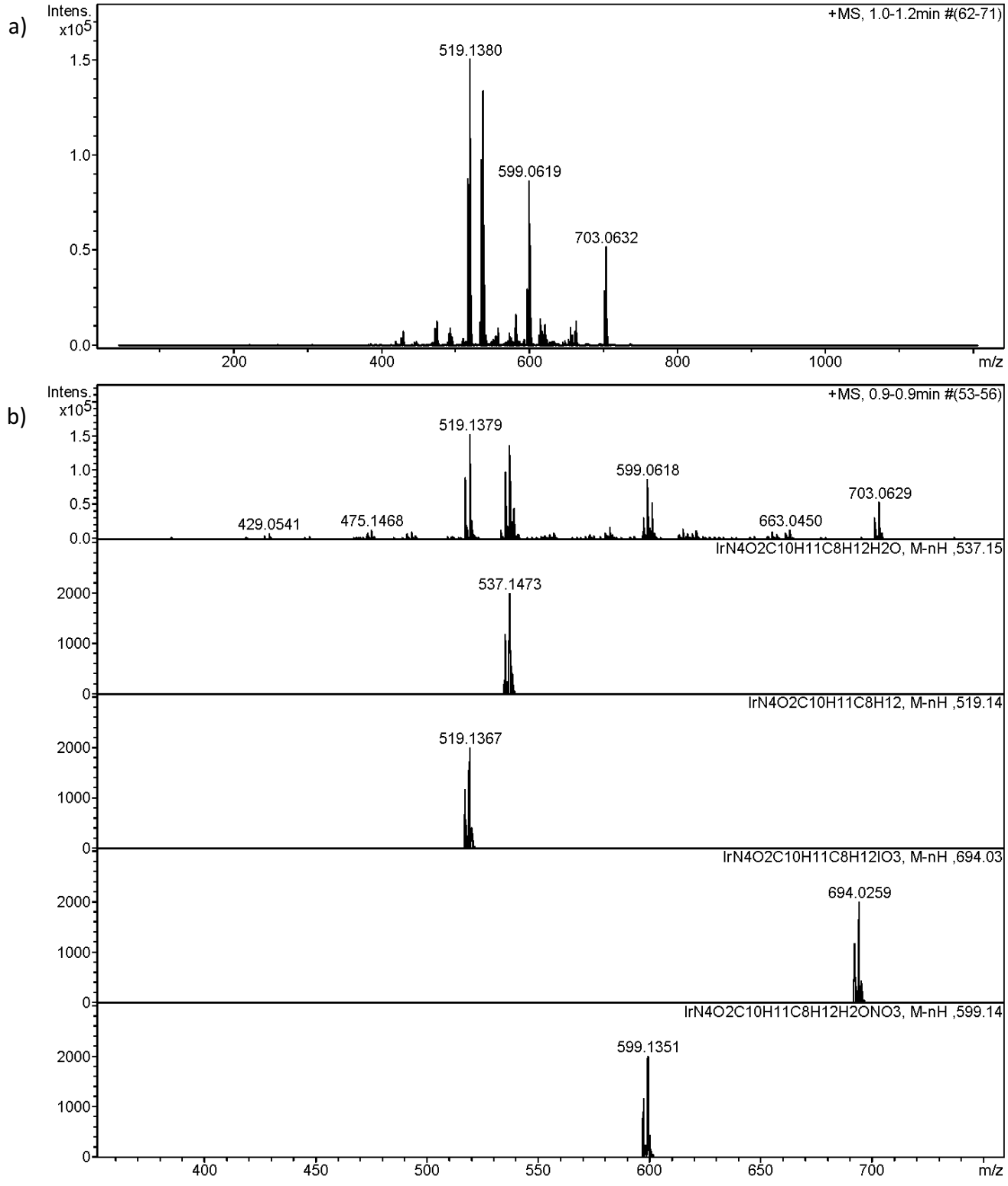

Figure S17. a) HRESI+-MS spectrum of **10**, b) Isotopic pattern for the most significant identified peaks.

10.- CAN-driven water oxidation by catalyst precursors 1 and 4: Mass Spectrometric studies.

[Cp*IrCl{$(MeIm)_2CHCOO$}] (**1**), (5 mg, 0.0085 mmo, in 5 mL of H_2O).

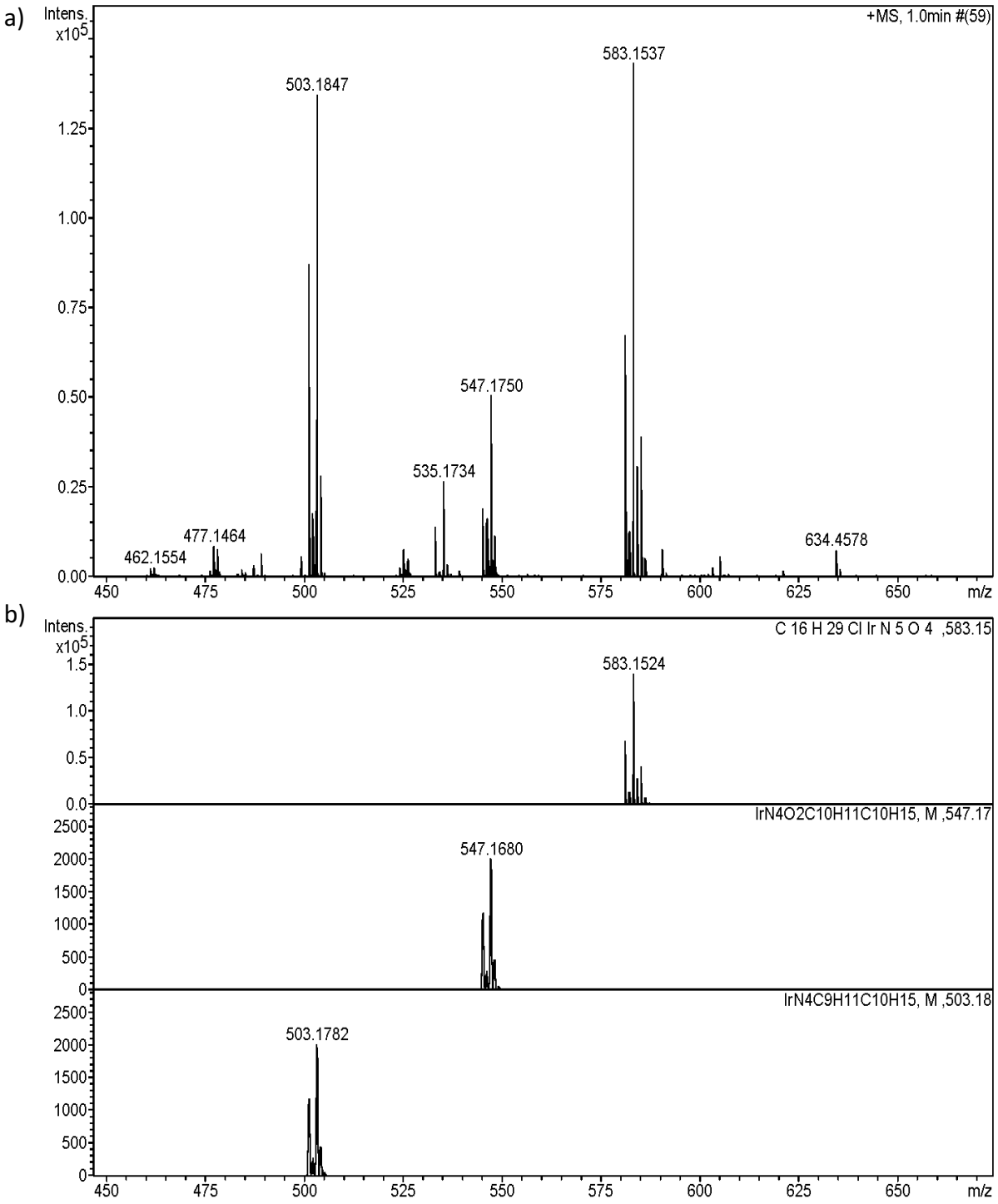

Figure S18. a) ESI+-MS spectrum of **1**, b) Isotopic pattern for the most significant identified peaks.

[Ir(cod){$(ImMe)_2CHCOO$}] (**4**) (5 mg, 0.0095 mmol, in 5 mL of H_2O).

a)

b)

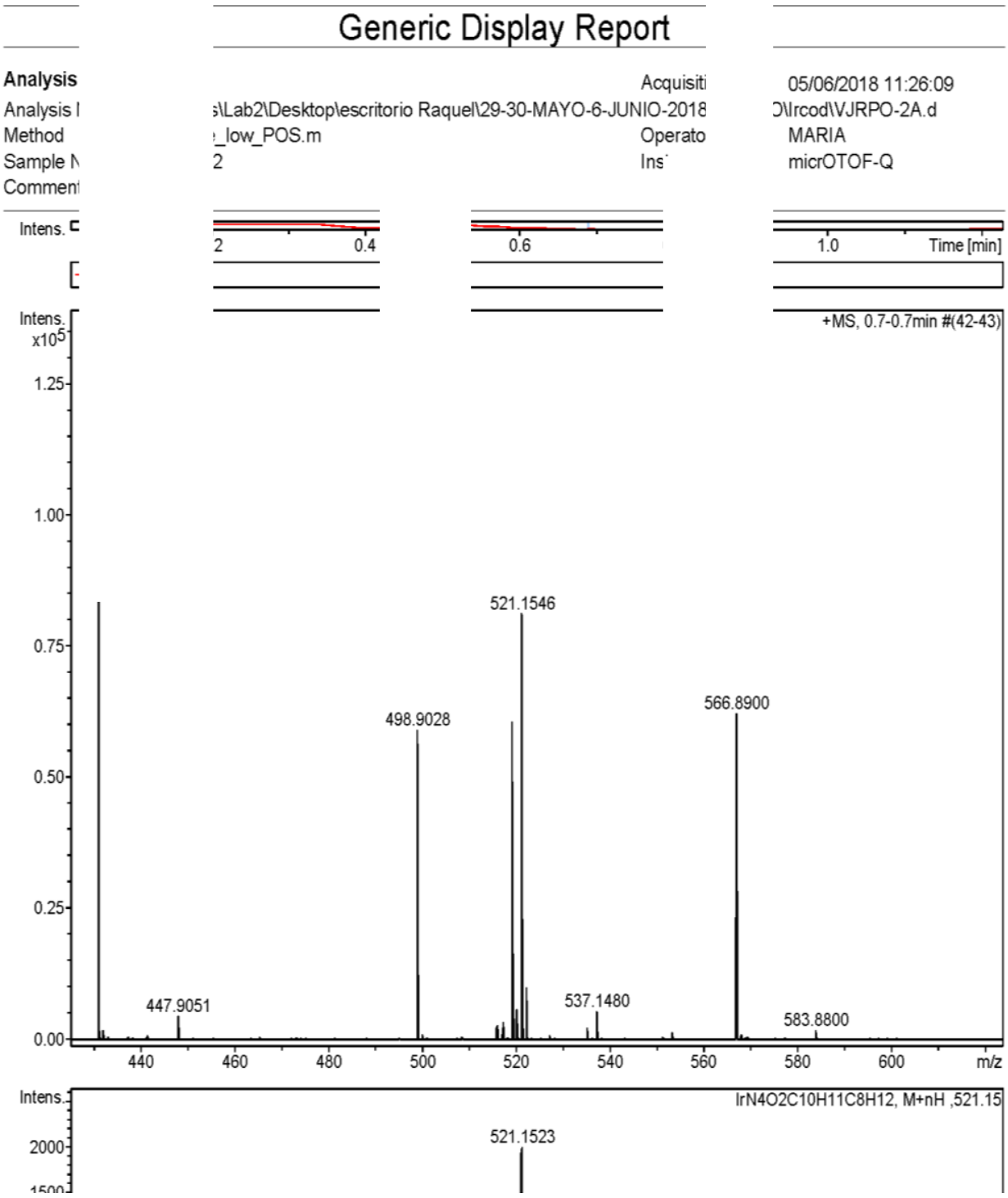

Figure S19. a) ESI+-MS spectrum of **4**, b) Isotopic pattern for the most significant identified peaks.

[Cp*IrCl{(MeIm)$_2$CHCOO}] (**1**) (5 mg, 0.0085 mmol in 5 mL of H_2O) + 50 equiv of $(NH_4)_2Ce(NO_3)_6$ (180,3 mg, 0.425 mmol).

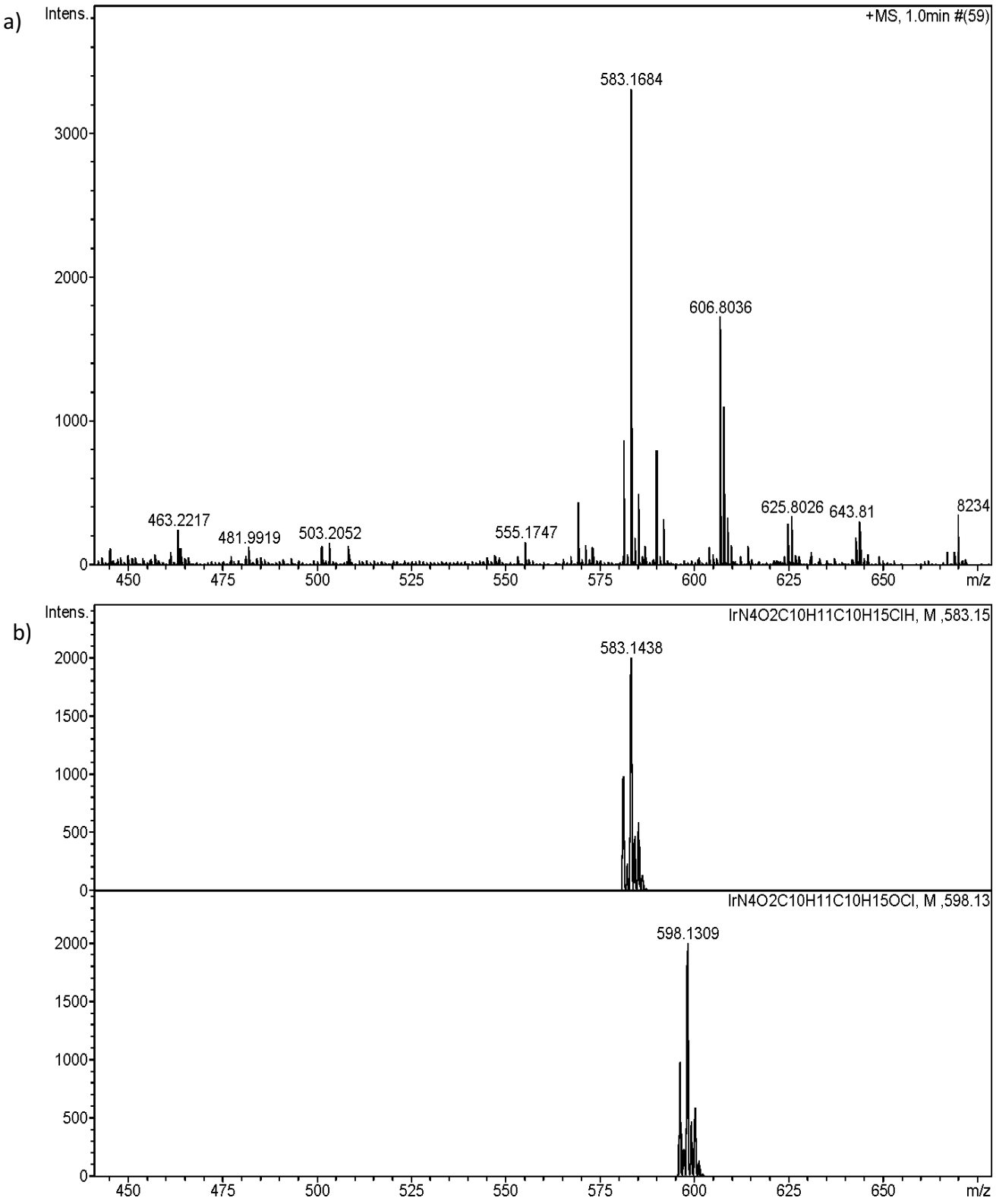

Figure S20. a) ESI+-MS spectrum of **1** at 24 h of reaction,, b) Isotopic pattern for the most significant identified peaks.

[Ir(cod){(ImMe)$_2$CHCOO)}] (**4**) (5 mg, 0.0095 mmol, in 5 mL of H_2O) + 50 equiv of $(NH_4)_2Ce(NO_3)_6$, (201.5 mg, 0.475 mmol). Mass spectra of water solutions of **4** treated with 50 equiv. of CAN:

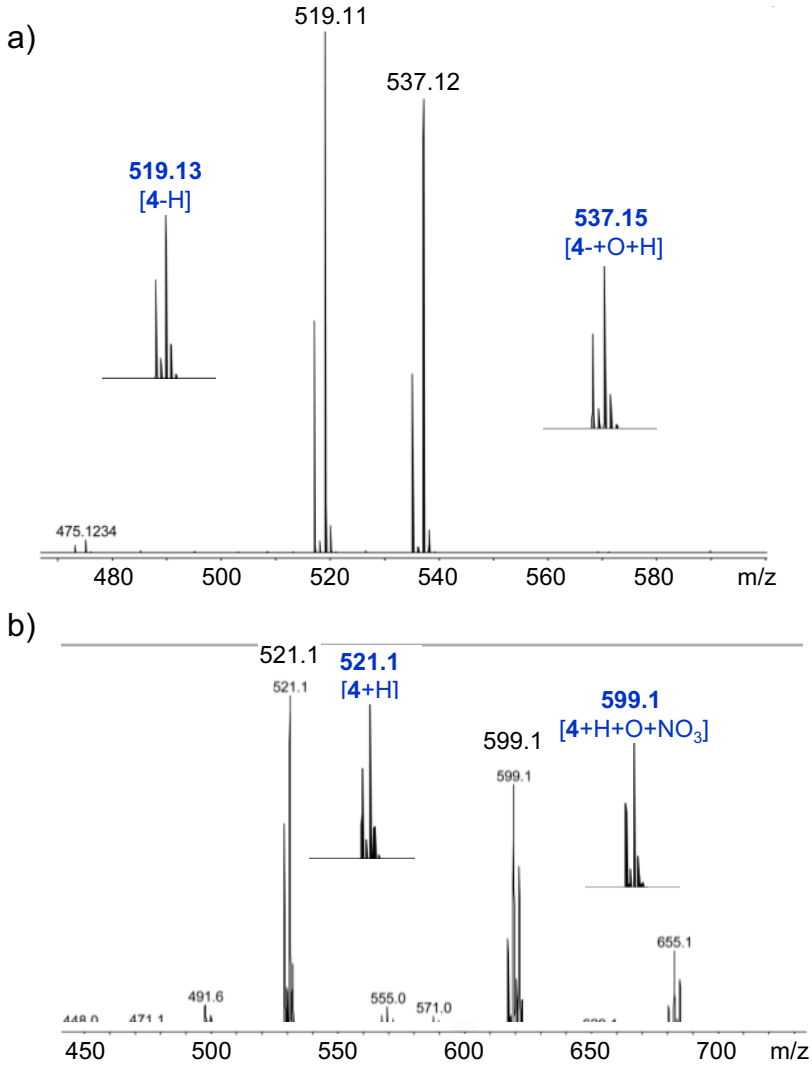

Figure S21. a) MS−ESI+ spectrum after 10 min, b) MS−MaldiToF spectrum after 24 h.

[Ir(cod){(ImMe)$_2$CHCOO)}] (**4**) (5 mg, 0.0095 mmol, in 5 mL of H_2O) + 50 equiv of $(NH_4)_2Ce(NO_3)_6$, (201.5 mg, 0.475 mmol). Mass spectra of water solutions of **4** treated with 50 equiv. of CAN:

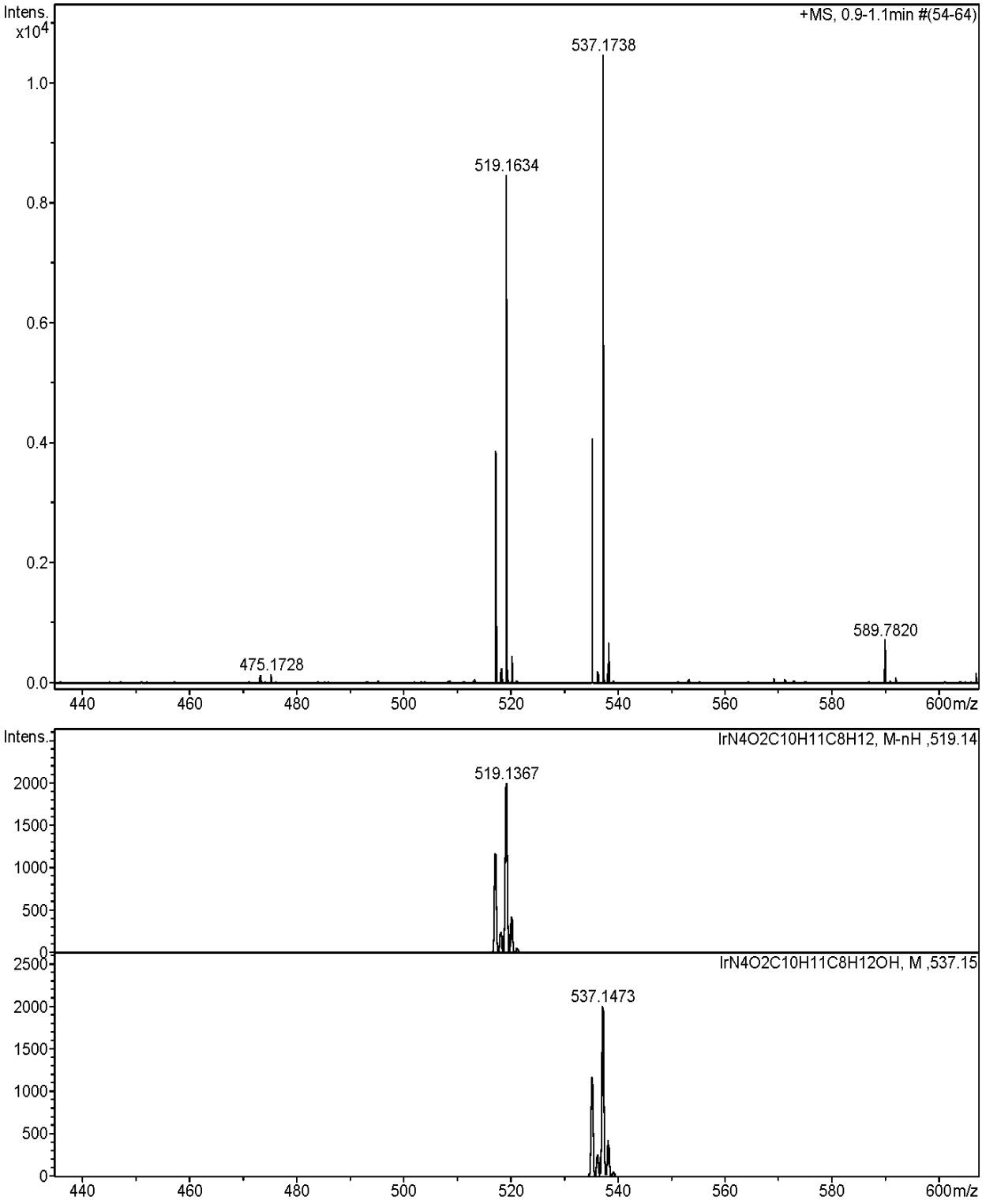

Figure S22. a) ESI+-MS spectrum measured at 24 h of reaction, b) Isotopic pattern of the most significant identified peaks.

11.- Electrochemical studies: Cyclic voltammograms (CVs) for 1 and 4 in water.

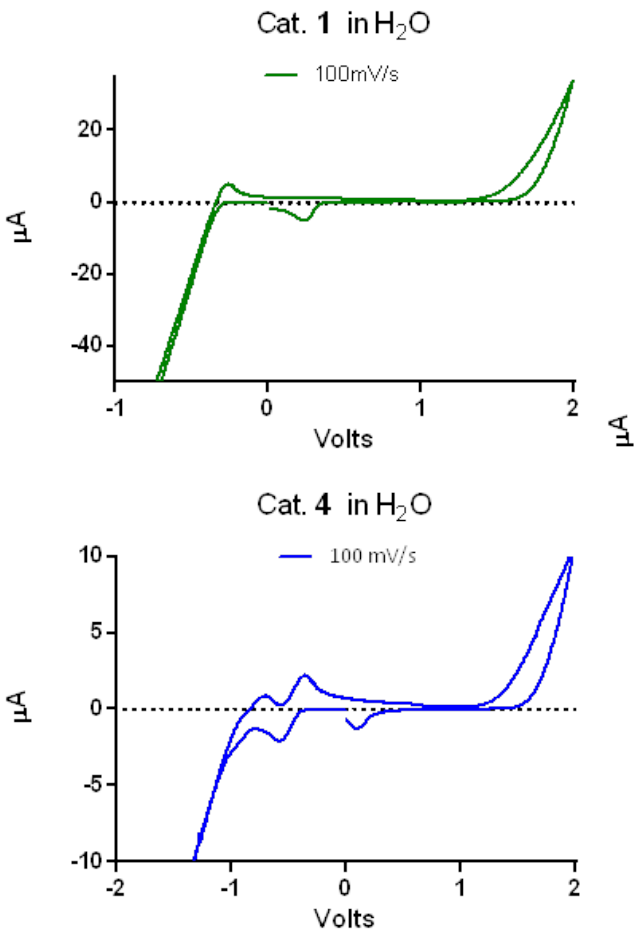

Figure S23. CVs for **1** and **4** in water at 100 mV/s

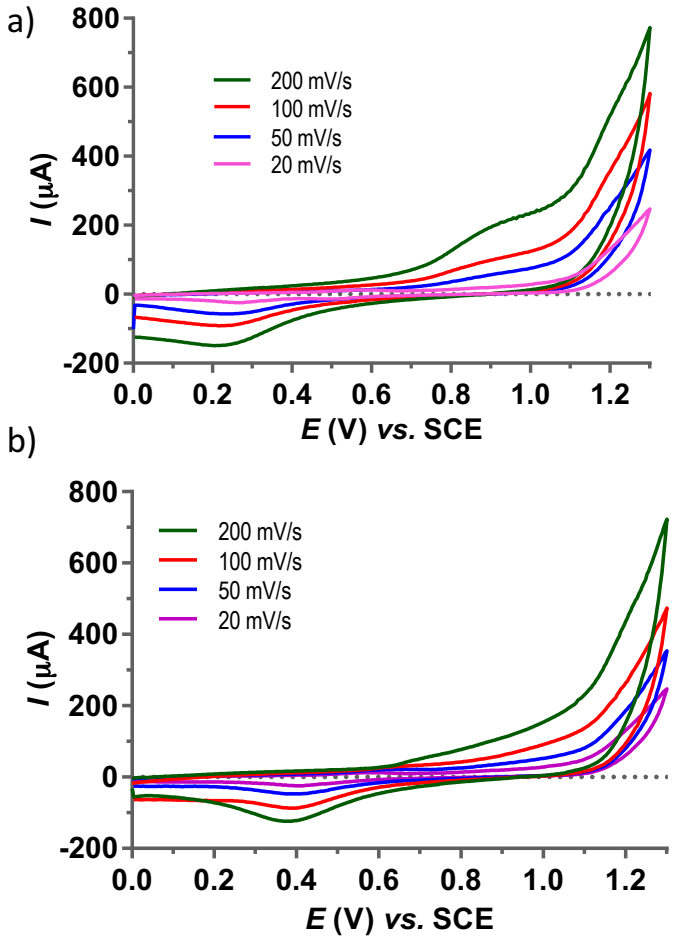

Figure S24. a) CV of **1** in water at pH = 7 at different scan rates; b) CV of **1** in water at pH = 1 at different scan rates.

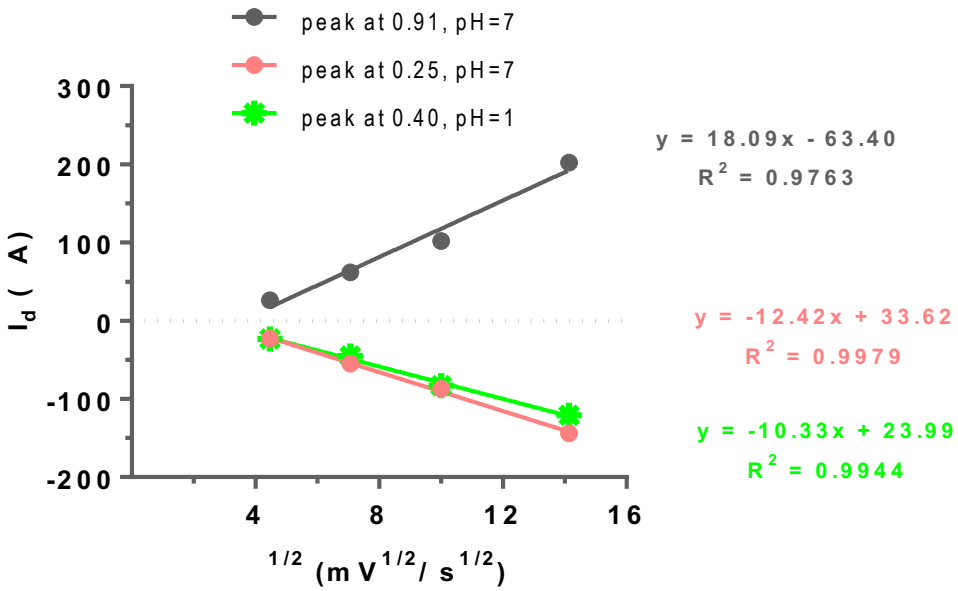

Figure S25. Representation of the peak current at E = 0.91 and 0.25 V (for pH = 7) and 0.40 (for pH = 1) *vs.* the square root of scan rate.